Development of Simulator for the Gamma-ray Satellite GLAST
(次期ガンマ線観測衛星 GLAST シミュレータの開発)

M1179023
平野 勝也

広島大学理学研究科物理科学専攻
素粒子実験・高エネルギー宇宙学研究室

February 22, 2001

Abstract

In this thesis, we developed a detector simulator for GLAST (Gamma-ray Large Area Space Telescope) using Geant4, which is a software toolkit to simulate physical processes between materials and high energy particles. For a preparation stage of a complete simulator for GLAST, we constructed a detector simulator which represents the geometry of the detector of a beam test carried out in 1999 – 2000 at SLAC (Stanford Linear Accelerator Center) to investigate the response of the test detector. We also evaluated the validity of the simulator to compare with the data of the beam test.

In this June, an experiment that launches a test detector on-board balloon is planed in order to test the performance of the detector in the space-like radiation environment. In this experiment, it is difficult to catch enough amount of celestial gamma-ray events because of limitation of observation time, thus four plastic scintillators (called "Active Targets") are placed above the detector. With these Active Targets, we can obtain gamma-rays generated at Target. Since many backgraund events due to cosmic-ray charged particles are expected, it is necessary to estimate a background as well as an event rate. Accordingly, we developed a model of cosmic-ray fluxes based on the data of the past experiments, and constructed the detector geometry of the balloon experiment based on the beam test simulator. Energy spectrum of cosmic-rays depends on the activity of the sun and the geomagnetic field, therefore we considered these effects to predict the flux at the place where the balloon experiment is carried out, and shot an expected cosmic-ray proton on the detector in the simulator. As a result, we find that about 200 π^0 decayed gamma-ray events are expected in the balloon experiment.

Contents

Chapter 1

Introduction

Since the discovery of a gamma-ray astronomical objects, X-ray and gamma-ray satellites tell us that there are a lot of high energy phenomena in the universe – such as active galactic nuclei, black hole candidates, pulsars involving jets, shock fronts of super nova remnants, high temperature plasmas in galaxies or clusters of galaxies, gamma-ray bursts, and solar flares. These indicate that high energy particles are accelerated in these objects, and thus the objects are "natural accelerators". What mechanism contributes to accelerating particles effectively, and where is the source of cosmic-ray particles? To understand the mechanisms of these natural accelerators, it is important to observe these objects with a high energy gamma-rays.

There are various important electromagnetic radiation processes in the gamma-ray astrophysics; synchrotron radiation between high energy electrons or positrons and magnetic field, non-thermal bremsstrahlung from high energy electrons, inverse compton scattering from the interaction between high energy electrons and photons, and the decay of π^0 meson produced by the interaction between cosmic-ray protons and interstellar medium. Therefore gamma-ray region is the most suitable to study high energy phenomena in the space.

The gamma-ray observation opened a new era by appearance of CGRO (Compton Gamma Ray Observatory) satellite in 1991. An on-board gamma-ray detector named EGRET (The Energetic Gamma Ray Experiment Telescope) has observed a few hundred gamma-ray objects. However it equips detectors based on old technologies, such as spark chamber, because of postponement of launch. A new project of gamma-ray observatory called GLAST (Gamma-ray Large Area Space Telescope) was proposed and started in 1995. This new satellite will discover more than ten thousands of gamma-ray astronomical objects with its superior sensitivity.

Table 1.1 shows the conparison of performances between EGRET and GLAST.

Quantity	EGRET	GLAST (Minimum Spec.)
Energy Range	20 MeV – 30 GeV	20 MeV – 300 GeV
Peak Effective Area	1500 cm^2	8000 cm^2
Field of View	0.5 sr	> 2 sr
Angular Resolution	5.8 degree (100 MeV)	<3.5 degree (100 MeV) <0.15 degree (>10 GeV)
Energy Resolution	10 %	10 %
Deadtime per Event	100 ms	<100 μs
Source Location Determination	$15'$	$< 0.5'$
Point Source Sensitivity	$\sim 1 \times 10^{-7} cm^{-2} s^{-1}$	$< 6 \times 10^{-9} cm^{-2} s^{-1}$

Table 1.1: GLAST specifications and performance compared with EGRET

Chapter 2

Gamma-ray Satellite GLAST

2.1 Overview of GLAST

GLAST (Gamma-ray Large Area Space Telescope) is a high energy gamma-ray satellite for observing celestial objects with wide energy bands from 20 MeV to 300 GeV. It is a collaborative project of America, Japan, Italy and France, and it will be launched by NASA. GLAST can measure the direction and energy of incoming gamma-rays simultaneously with a e^+e^- pair-conversion type detector. GLAST can detect celestial gamma-rays with excellent spatial resolution down to a few arcminutes, and has a quite wide field-of-view, covering about 20 % of the whole sky. GLAST has many advantages in energy range, field of view and spatial resolution compared to the previous gamma-ray detector EGRET (The Energetic Gamma Ray Experiment Telescope) on board CGRO (Compton Gamma Ray Observatory) satellite which was operated in 1991 – 2000. The sensitivity is expected to reach 50-100 times higher than that of EGRET.

GLAST consists of identical 4 $\times$ 4 modules, each of which is called "tower". The tower is divided into three parts; a tracker part (TKR), a calorimeter part (CAL), and an anti-coincidence detector part (ACD). This multi-module configuration reduces the load of the trigger system and the dead time, keeps the redundancy, and makes the system constructed easily. Figure 2.1 shows the module structure of GLAST schematically.

One TKR part has 36 layers of silicon microstrip detectors (SSDs) and thin lead sheets. Incoming gamma-rays are converted to e^+e^- pair at one of the lead sheets. The track of produced e^+e^- pair is recorded by the SSDs, and thus the direction of incoming gamma-rays can be determined. One CAL part consists of arrays of 80 long narrow CsI crystals, and incoming electrons and positrons produce electromagnetic shower in it. Each CsI crystal can determine the deposited energy and measure the average position of energy deposits by reading out its scintillation light from both side of the crystal with photo-diodes. In this way, the detector can measure direction and energy of each gamma-ray simultaneously. The ACD system consists of plastic scintillators placed to cover the front and side of the main detector (TKR/CAL). We can remove events of charged particles that hit both ACD and main detector.

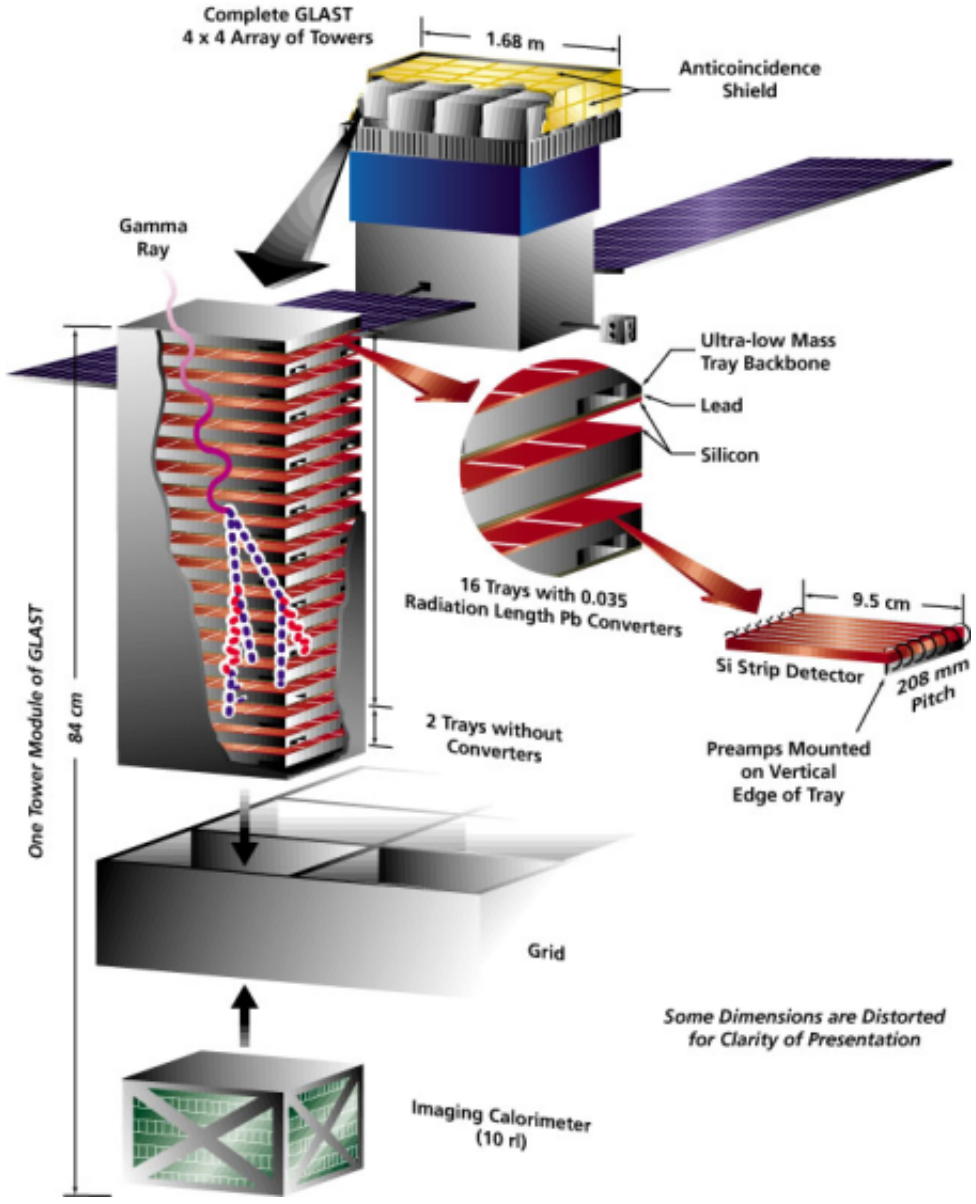

Figure 2.1: Schematic view of GLAST module structure

2.2 Silicon Microstrip Detector

The wide energy band, high spatial resolution, and large field of view of GLAST are achieved by utilizing the SSD as a tracker part. SSDs for GLAST have been studied and developed mainly in Hiroshima University, and have quite a high accuracy of tracking and long been used in high energy physics experiments at the nearest point of vertex, where the detectors are exposed to strong radiation environment. Thus SSD has a good tolerance for radiation and withstand a high trigger rate. In addition, there are many knowledges and technologies such as fast readout circuits that work with very low power consumption. These features of SSDs are suitable for a satellite experiment. The schematic view of

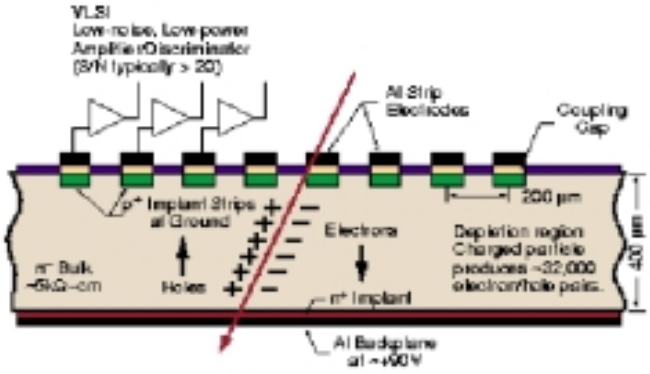

Figure 2.2: The schematic view of silicon microstrip detector

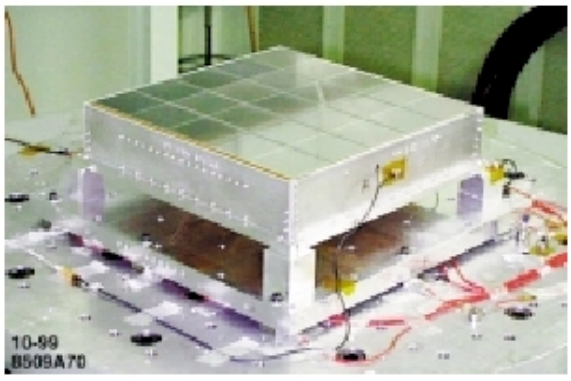

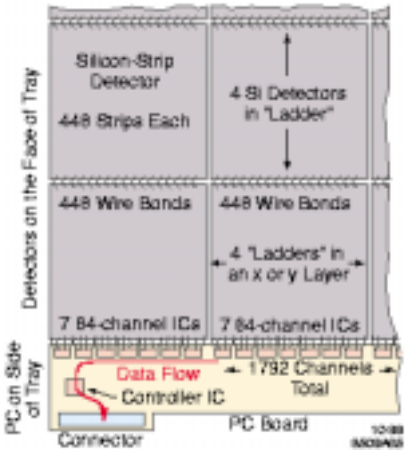

Figure 2.3: The picture of silicon tray (left) and schematic view of SSD configuration

section of SSD is shown in Figure 2.2.

The size of a SSD plate utilized in GLAST is 89.5 mm×89.5 mm×0.4 mm diced from one silicon wafer, and there are 384 strips with the strip pitch 228 μm in one SSD. About 10,000 SSDs will be used in whole GLAST. Figure 2.3 shows a picture of a tray of TKR and the schematic view of SSD configuration.

2.3 Comparison with Other Instruments

Although the structure of detectors is similar to that of EGRET, GLAST will show much improved performance. This is mainly due to the high accuracy of tracking by SSDs in TKR. GLAST uses SSDs about 100 m^2 in total, so that we can obtain both a few arcminutes spatial resolution and a large field of view which covers about 20 % of the whole sky. Integrated circuits and multiple trigger systems are under development to process an expected high rate trigger. The excellent sensitivity of GLAST, over 50 times than that of EGRET, will be achieved by combining these new technologies.

The distinctive feature of GLAST is a large field of view and a good angular resolution. It is impossible for telescopes with lens or reflecting mirror to achieve these two features simultaneously. The typical field of view of X-ray reflecting mirrors is about a few times 10 arcminutes, and that of optical telescopes are not so different. GLAST detects gamma-rays by tracking the e^+e^- trajectory, and thus can determine the incident direction of gamma-rays coming with a large angle. Figure 2.4 shows the conparison of basic performances between GLAST and EGRET.

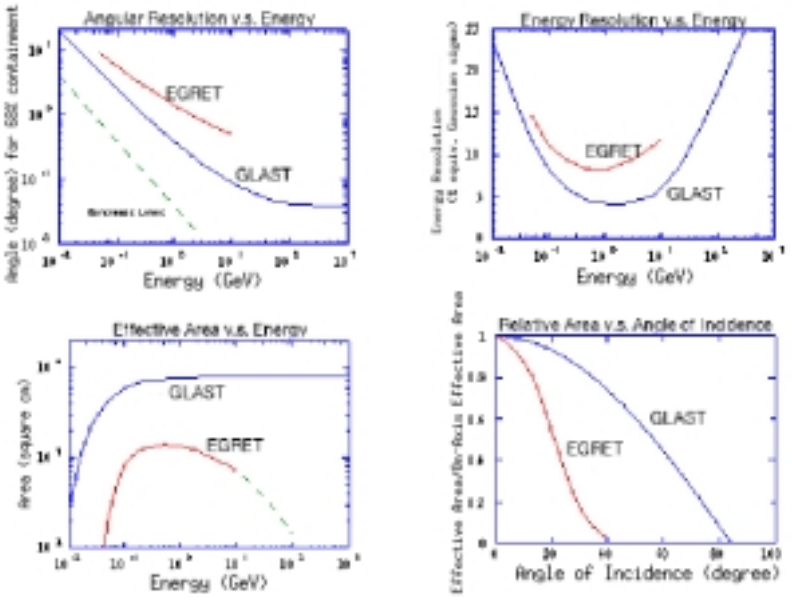

Figure 2.4: Basic performance of GLAST compared with EGRET

2.4 Calibrations of the Detector

GLAST detector is now under development, and a beam test using the beam from accelerator was performed for one tower (it is called BTEM, Beam Test Engineering Model) at Stanford Linear Accelerator Center (SLAC) in 1999 – 2000. This beam test focused on the study of data acquisition performance, validation of old Monte Carlo simulations (called GLASTSIM) for on-axis and off-axis incident beams. The incident particles used in the beam test is positrons, hadrons, and tagged photons in various energies. Figure 2.5 shows a picture of the detector in the beam test. The result of the data analysis is reported as Eduardo et al.[3]

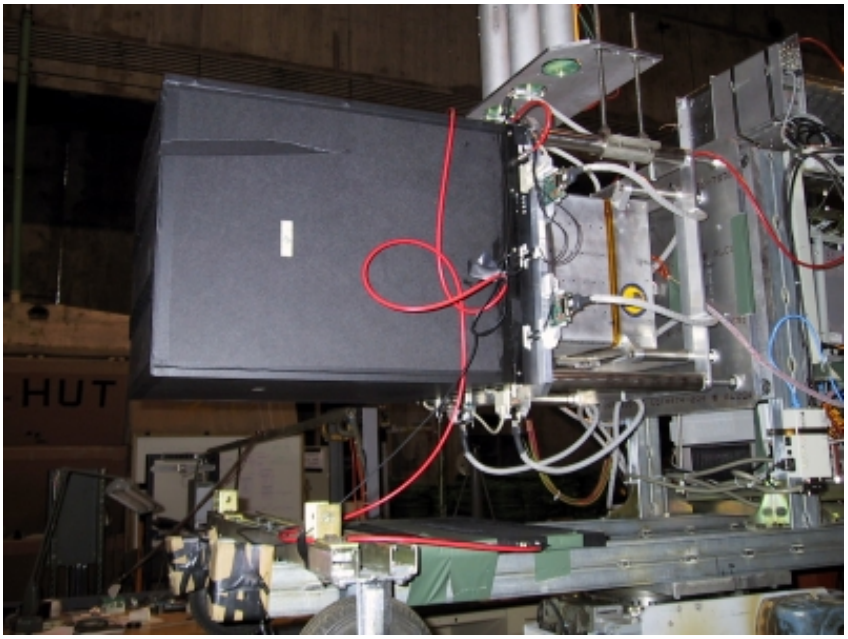

Figure 2.5: Picture of the detector in the beam test

In addition to the beam test, a balloon experiment is planned in June 2001 to confirm the detector performance in the environment that is almost the same as the space. The detector is almost identical to that of the beam test, but some incomplete layers (which lack SSDs) are removed to reduce the total weight. In the balloon experiment, there are few celestial gamma-ray events due to the limitation of the observation time. Thus external active targets which consist of plastic scintillator and photomultiplier tubes (PMTs) are additionally installed to the tower; when cosmic-ray protons hit the targets, induce inelastic scattering, and produce π^0 mesons, generated π^0 will be immediately decayed into gamma-rays. Thus we can obtain many useful tagged gamma-ray events whose incident direction is identified.

2.5 Objectives of This Thesis

An accurate simulator is needed to estimate the performance and detector design, and to achieve the above excellent sensitivity of GLAST. In this thesis, we developed a detector simulator of GLAST,for the beam test and the balloon test. At first, we constructed a geometry of one tower of GLAST module which was used in the beam test and validated the simulator by comparing with the real experiment. Then, we constructed a geometry of balloon experiment and the model of the cosmic-ray of the balloon flight, in order to represent a radiation environment. Finally, we estimated the event rate on the balloon flight by using the simulator.

Chapter 3

Construction of the Detector Geometry with Geant4

3.1 Overview of Geant4

Geant4[2] is an Object-Oriented toolkit for the detector simulation to reproduce the interaction between high energy particles and matters in detectors. It is now widely applied to high energy physics, medical technology, accelerator and astrophysics studies.

Geant4 provides a complete set of tools for the detector simulation: geometry, tracking, physical processes, particle gun, event and track management, visualization and user interface. Multiple implementation of physics processes and models are available.

The flow-chart of the typical simulator with Geant4 is explained in Figure 3.1.

3.2 Detector Geometry

As we mentioned in section 2.1, GLAST has 4×4 modules called tower, consists of TKR, CAL, and ACD.

In this study, we constructed a geometry of one tower of GLAST detector that corresponds to the beam test model in 1999 – 2000 and the balloon flight model in 2001. We referred to specification documents ("GLAST Testbeam Users guide version 1.5"[4] and "Geometry for the TRACKER to update .XML"[5]) to configure the detector in the simulator. For densities and mass numbers of elements and materials, we used the value in "The European Physical Journal" (2000)[6].

Below we describe details of the geometry of each part.

Tracker (TKR) Each of the 16 identical TKR modules consists of 16 x,y planes of SSDs, lead converter foils, and the associated readout electronics, all supported by a carbon-composite structure.

The support structure for the detectors and converter foils is composed of a stack of 17 composite panels, call "trays," aligned at the four corners and held in compression

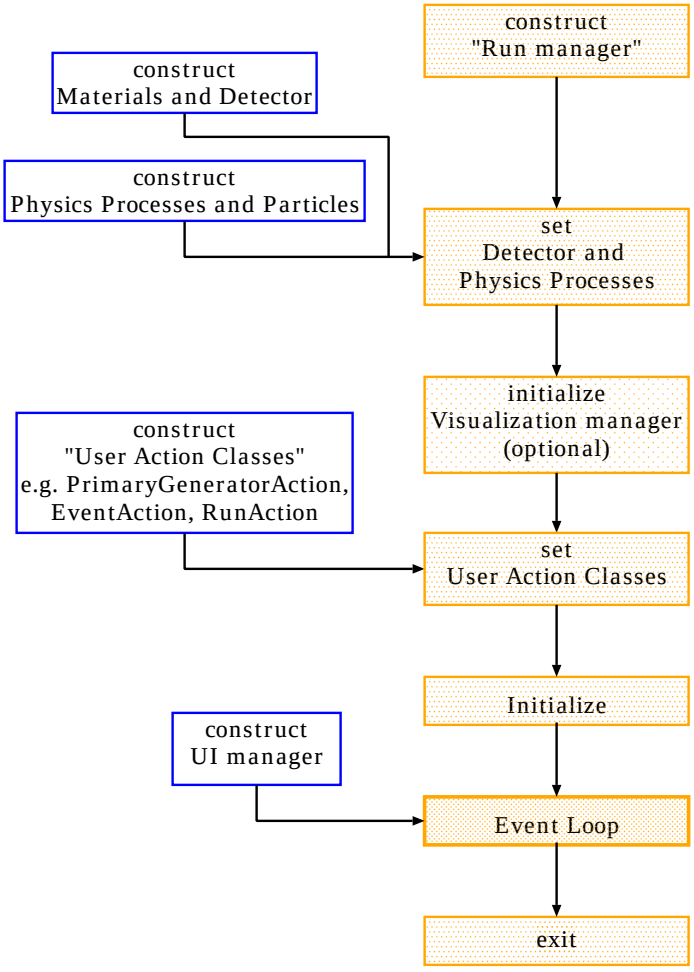

Figure 3.1: Flow-chart of main() function of the simulator with Geant4

by cables threaded through the corners. In Figure 3.2, the schematic view of a tray is shown. Sidewalls provide additional strength, protect the electronics, and conduct heat to the TKR base. The tray structure is a low-mass carbon-composite assembly composed of a closeout, face sheets, and vented honeycomb core. Carbon-composite is chosen for its long radiation length, high modulus-to-density ratio, and thermal stability.

A tray consists of a "y" layer of SSD on the bottom of one tray together with the "x" SSD layer on the top of the tray just below, with only a 2-mm separation. The lead converter layer lies immediately above the "y" layer. There are 11 x,y planes from the top of the TKR with 3.5% radiation length converters ("standard trays" or "front section"), followed by 3 x,y planes with 25% radiation length converters ("super GLAST" or "back section"). The last three trays have no converter foils ("no lead tray"). Figure 3.3 shows the arrangement of trays.

For the beam test, SSDs with two different sizes were used ("4-inch" and "6-inch",

see Figure 3.3), but strip width, strip pitch and number of strips are the same among all detectors. The number of ladder per tray and their type of wafer is described in Ref. [4][5]. Not all trays and ladders are fully equipped. The trays 9 to 17 are not fully equipped with SSDs, and we call these layers "a incomplete layer".

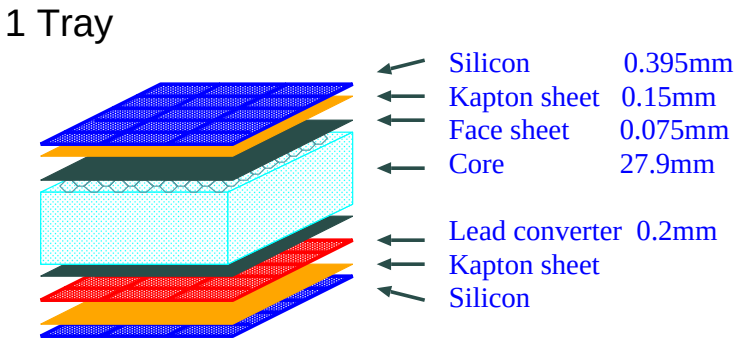

Figure 3.2: Schematic view of a tray

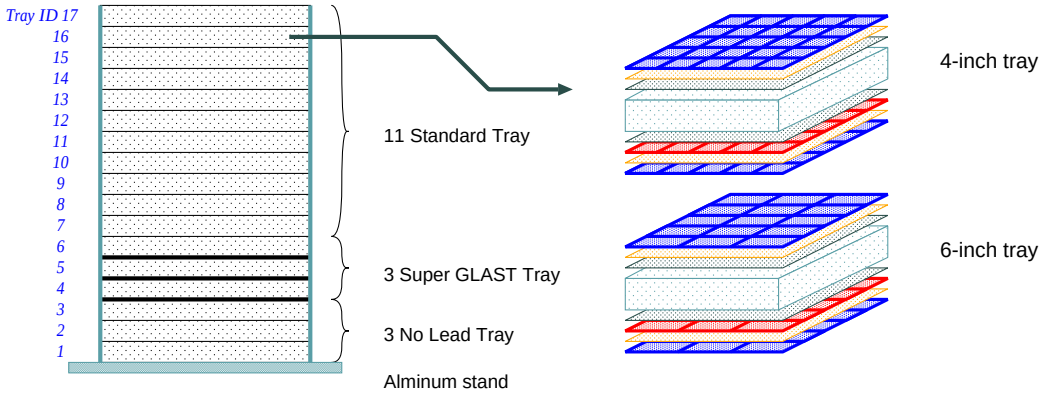

Figure 3.3: Schematic view of a tower

In constructing the detector geometry in the simulator, we arrange all the materials according to the configuration described above. Table 3.1 shows the sizes of each material we included in the simulator. We register the whole region of silicon detectors as "sensitive detector" where Geant4 records particle tracks. Actual SSD has insensitive regions in the periphery but we don't consider it in the simulator because the region is less than a few percent. Lead converters are placed in same way with SSDs. They are smaller than SSDs slightly, and we placed them between x and y planes. We represent Kapton sheets and Face sheets by materials in table 3.1. Although core is composed of the honeycomb structure, we constructed it as a box of aluminum with a density 0.017 g/cm^3, which is 0.6 % of normal aluminum.

Material	Elemental composition	Density [g/cm^3]	Size
4-inch Silicon	Si	2.330	64.0×64.0×0.395 mm^3
6-inch Silicon	Si	2.330	64.0×106.8×0.395 mm^3
4-inch Lead	Pb	11.35	62.4×62.4×0.20 mm^3
6-inch Lead	Pb	11.35	62.4×105.2×0.20 mm^3
Lead for super GLAST	Pb	11.35	62.4×105.2×1.6 mm^3
Core	Al	0.017	330.2× 330.2×27.9 mm^3
Kapton	$C_{10}H_2O_4N_2Cu$	1.420	330.2×330.2×0.15 mm^3
Facesheet	C	1.20	330.2 ×330.2×0.075 mm^3

Table 3.1: Materials included in TKR

There are some other matters around TKR. Aluminum side walls surround TKR, an aluminum stand is put under TKR, and light-shield boxes cover the whole TKR (and ACDs). These materials are also included in the simulator. Elemental compositions, densities, and dimensions of these materials are summarized in Table 3.2.

Material	Elemental composition	Density [g/cm^3]	Size
aluminum side wall	Al	2.70	330.2×545.9×1.5 mm^3
aluminum stand	Al	0.017	528.3×528.3×22.6 mm^3
light-shield wall	C	2.26	510×671×5 mm^3

Table 3.2: Materials around TKR

Calorimeter (CAL) In CAL, a long narrow stick of CsI crystal is adopted. One layer consists of ten CsI crystals arranged in side by side, and eight layers make up the whole CAL. Each layer is arranged in two perpendicular directions in order to get the x and y position information. In the simulator, we divide a CsI crystal into ten regions to simulate the position information of energy deposition. There are Polystyrene films for reflector and a rubber for absorbing the shock between each layer of CsI. The material of Polystylen is C_8H_8, and that of rubber is C_4H_6. In order to record the deposited energy, we register all CsI crystals as the sensitive detector. Figure 3.4 shows the schematic view of CAL.

There are frames of aluminum which encloses CAL to support it. To represent these frames in the simulator, we placed aluminum boards whose density is 20 % of usual aluminum around CAL. Informations of the materials in CAL are summarized in Table 3.3.

Anti Coincidence Detector (ACD) GLAST includes ACDs to identify the background events caused by charged particles. ACD consists of twelve plastic scintillator

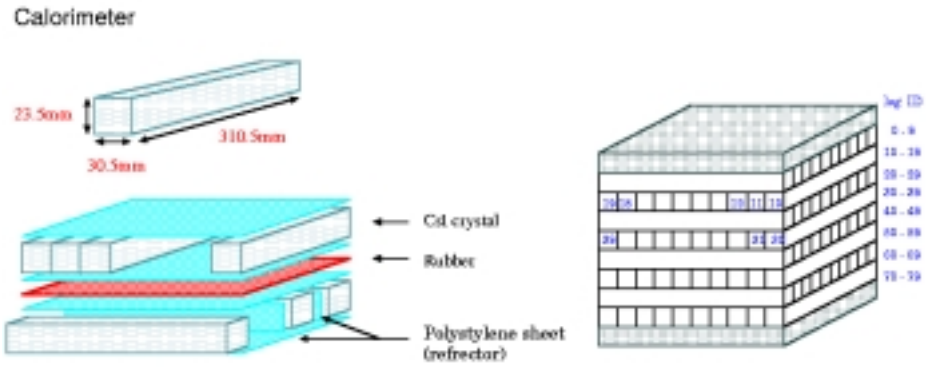

Figure 3.4: Schematic view of CAL

Material	Elemental composition	Density [g/cm^3]	Size
CsI crystal	CsI	4.53	30.5×23.5×310.5 mm^3
Polystyrene	C_8H_8	1.032	thickness 0.42 mm
rubber	C_4H_6	1.0	thickness 2.62 mm
CAL support frame	Al	0.54	thickness 20 mm (top) and 8 mm(side)
ACD	C_8H_8	1.032	thickness 10.0 mm

Table 3.3: Material included in CAL and ACD

boards, and they are arranged at the top and side of the TKR as double panels. The material of plastic scintillator is Polystylen (C_8H_8). We placed twelve plastic scintillator panels around the TKR and all panels are registered as sensitive detector. Photomultiplier tubes (PMTs) which take out the signal of ACDs are not placed in the simulator.

Figure 3.5 shows the geometry of the tower constructed in the simulator.

3.3 Physical Processes Specified in the Simulator

Physical Processes Geant4 calculate the track of particles separating into contiguous segments bounded by either interaction or sampling distance close to the mean free path of the particle. One must specify the physical process and particles to simulate the interaction. The processes we included are :

- General processes
  decay
- ElectroMagnetic processes
  photo electric effect, compton scattering, pair conversion, ionization, bremsstrahlung,

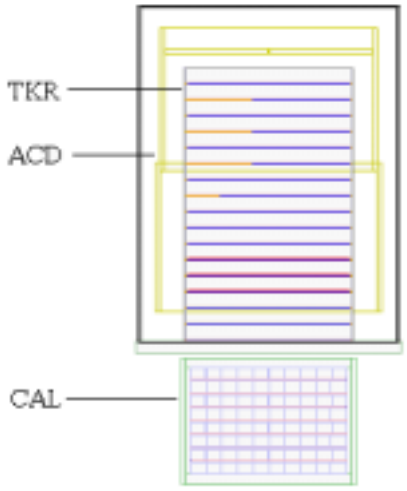

Figure 3.5: Side view of the tower constructed in the simulator with Geant4

multiple scattering, and annihilation

- Hadronic processes
  elastic scattering and inelastic scattering

We set these processes in the simulator according to the example code which is distributed from the Geant4 project team.

Geant4 calculate the particle track until its energy becomes 0, and in the process of the calculation, the particle losses its energy and product secondary particles. Users can set the cut value for this secondary particle production in terms of range; a particle with range below this value is not generated in simulation, but its energy is deposited locally in the material. We determine the cut value to be 0.1 mm for most of the particles. To avoid many trajectories of knocked-out δ-ray electrons, we set the cut value for electron 0.4 mm.

Data Output One can get the hit information of materials which registered as a sensitive detector of Geant4 for each run. The format of output data is ASCII, and the information we output is described as follows:

- TKR
  The sample of output data is shown in Figure 3.6. In the figure, EventNo means the number of each event, NoTrackerHit gives a number of hit SSDs, ID gives the ID number of SSD, ParSpc gives a particle species, TrkLen gives the length of track in the material, XYZi/XYZo gives the input/output position, DepE gives the energy deposition, and ParE gives the total energy of the particle at the input point.

- CAL
  The sample is shown in Figure 3.8.
  number of hit CsI crystals, deposit energy, position of the energy deposition, and total deposited energy in CAL.

- ACD
  The sample is shown in Figure 3.7.
  number of hit ACD panels, its ID number, and total deposit energy in each panel.

```
EventNo= 1
 NoTrackerHit= 0
EventNo= 2
 NoTrackerHit= 4
  ID= 25  ParSpc= proton  TrkLen= 0.412103  XYZi= -22.4675  -151.875  387.193
   XYZo= -22.355  -151.909  386.798   DepE= 0.117856  ParE= 4513.2
  ID= 24  ParSpc= proton  TrkLen= 0.41212  XYZi= -21.5969  -152.137  384.137
   XYZo= -21.4844  -152.171  383.743   DepE= 0.103989  ParE= 4513.08
  ID= 23  ParSpc= proton  TrkLen= 0.412142  XYZi= -13.3437  -154.615  355.193
   XYZo= -13.2311  -154.649  354.798   DepE= 0.121419  ParE= 4511.56
  ID= 22  ParSpc= proton  TrkLen= 0.412145  XYZi= -12.4726  -154.878  352.137
   XYZo= -12.36  -154.912  351.743   DepE= 0.114469  ParE= 4511.44
  ....
```

Figure 3.6: Sample of output data of TKR

```
EventNo= 1
 NoAntiHit= 2
  ID= 7    DepE= 4.80374
  ID= 13    DepE= 4.07143
EventNo= 2
 NoAntiHit= 3
  ID= 10    DepE= 6.40388
  ID= 12    DepE= 1.06115
  ID= 22    DepE= 8.56701
  ....
```

Figure 3.7: Sample of output data of ACD

```
EventNo= 1
 NoCalHit= 0
  ....
EventNo= 47
 NoCalHit= 11
 LogID= 7  DepE= 1.40993  Pos= 0 -15.525 0
 LogID= 8  DepE= 7.93742  Pos= 0 -15.525 0
 LogID= 16  DepE= 14.9298  Pos= 0 108.675 0
 LogID= 28  DepE= 13.495  Pos= 0 -46.575 0
 LogID= 36  DepE= 14.5518  Pos= 0 108.675 0
 LogID= 48  DepE= 12.3613  Pos= 0 -46.575 0
 LogID= 49  DepE= 2.09004  Pos= 0 -46.575 0
 LogID= 56  DepE= 16.8438  Pos= 0 139.725 0
 LogID= 69  DepE= 13.9767  Pos= 0 -46.575 0
 LogID= 76  DepE= 7.61849  Pos= 0 139.725 0
 LogID= 77  DepE= 1.73307  Pos= 0 139.725 0
  TotCalE= 107.68
  ....
```

Figure 3.8: Sample of output data of CAL

3.4 Validation of the Simulator

The validity of the simulator we constructed is investigated by Ogata[16], Sato[17], and Azechi[18]. The validation item that have already been performed are summarized as follows.

- The energy loss along per unit length follows the formula of Bethe-Bloch for protons.
- The energy loss distribution follows the Landau distribution.
- The e^+e^- conversion probability in the simulator agrees with the numerical calculation.
- The distribution of hit multiplicity agrees with the data of beam test.
- The reconstruction of the incident direction of gamma-rays agrees with the beam test data.

Chapter 4

Construction of a Cosmic-ray Simulator

4.1 Cosmic-ray Simulators

In June 2001, a balloon experiment for GLAST will be carried out at Palestine in Texas, USA, to test the performance of the detector in space-like environment. The simulator for the balloon experiment is needed to decide the design of detector and estimate the number of useful events and backgrounds. Furthermore, cosmic-ray simulator is needed for the estimation of backgrounds of the GLAST flight model, which is very important for the analysis of faint objects and diffuse sources. Therefore we constructed the cosmic-ray simulators whose outputs are fed into the detector simulator.

4.2 Overview of Cosmic-rays

Cosmic-rays are high energy particles that come from outside the solar system. The species of cosmic-rays are protons, helium nuclei, heavy ions, electrons and positrons. The energy of cosmic-rays widely distributes from a few times 10 MeV to more than 10^{20} eV.

Cosmic-rays come to the earth in the following way: (1) particles are accelerated by high energy astronomical objects, (2) propagating the interstellar space and coming to the solar system, (3) "modulated" by the solar wind, (4) entering the atmosphere of the earth and cut at the lower energy, and (5) interacting with molecules in the air and creating secondary particles.

Thus cosmic-rays are separated into two components: "primary" and "secondary". The primary is a component of cosmic-rays which come from outside the earth directly, and the secondary is a component produced in the atmosphere by interactions between the primary cosmic-rays and molecules of the air. The secondary cosmic-rays are also called "albedo". The upward-moving (goes away from the earth) albedo is called "splash albedo", and the downward-moving (come to the earth) is called "re-entrant albedo".

Since cosmic-rays have a charge, they are affected by the activity of the sun and the geomagnetic field. We describe each effect below.

1. Intrinsic cosmic-ray spectra If particles are accelerated in some way, they form certain spectrum. It is said that the energy spectrum of this early stage of cosmic-rays follows a power law; $\sim E^{-2.3}$, where E denotes energy of the particle.

2. Propagating in the interstellar space Cosmic-ray particles propagate in the interstellar space and come into the solar system. High energy particles would escape from the galaxy and the energy spectrum becomes steeper, $\sim E^{-2.7}$.

3. Solar modulation Cosmic-rays entering the solar system are "modulated" by the solar wind, which is an expanding magnetized plasma flow ejected from the sun. The solar wind disturbs the magnetic field, and then the disturbance acts as a scattering body. The lower energy cosmic-rays are thus decelerated and partially excluded.

In the standing state, the number of cosmic-rays entering from out of the solar system is in balance with that of ones scattered by the solar wind, and therefore the diffusion equation of the cosmic-ray particles can be represented as

$$D\frac{dn(r)}{dr} = Vn(r), \qquad D = \frac{1}{3}\lambda v, \tag{4.1}$$

where λ is a mean free path in the scattering body (disturbance of the magnetic field), v is a velocity of the cosmic-ray particle, V is the velocity of the solar wind, $n(r)$ is a density of cosmic-ray particles at the distance r from the sun, and D is a diffusion coefficient.

There is a significant anticorrelation between solar activity (which has an eleven-year cycle) and the intensity of the cosmic rays with energies below about 10 GeV. To represent the differential energy flux of cosmic-ray particles concerning the solar modulation in a certain place r, and time t, the model called force-field approximation is available[14]:

$$\frac{J(r,E,t)}{E^2 - {E_0}^2} = \frac{J(\infty, E + e\Phi)}{(E + e\Phi)^2 - {E_0}^2} \tag{4.2}$$

where E and E_0 is the total and the rest energy of the particle, respectively, and $\Phi(r,E,t)$ is a potential energy or energy loss experienced in coming from infinity. The empirical value of Φ is about 540 MV at solar minimum and 1100 MV at solar maximum.

4. Effect of the magnetic field around the earth When cosmic-rays approach the earth, low energy cosmic rays are affected by the geomagnetic field; some particles cannot penetrate the air due to the Lorentz force, and go away outside the earth. The strength of geomagnetic field is often represented as a "geomagnetic latitude" θ_M ([rad] or [degree]) which is defined to be zero at the geomagnetic equator.

In the magnetic field B, the Ramour radius of the particles which have a momentum p and a charge Ze, can be expressed as

$$r \propto \frac{pc}{Ze}\frac{1}{B} = R\frac{1}{B}, \tag{4.3}$$

where c denotes the light speed and $R = pc/Ze$ is called rigidity.

As concerned as the trajectory of charged particles in the magnetic field of the earth, it can be said qualitatively :

1. Small momentum (small rigidity) particles are highly curved because their Ramour radius is small, and thus they will be bended easily.

2. Any particles running along the geomagnetic field line (small geomagnetic latitude) can run straightly and hence even small rigidity particles can reach the surface of the earth.

3. On the contrary, particles coming from the perpendicular of the geomagnetic filed line (large geomagnetic latitude) are highly curved and thus only large rigidity particles can penetrate the air.

Accordingly, the observed energy spectrum of cosmic-rays exhibits a low energy cut-off which depends on the geomagnetic latitude. Generally, cosmic-ray particles with an energy of less than about 10 GeV strongly suffer the influence of the geomagnetic field.

5. Production of secondaries Primary cosmic-rays interact with molecules of the air and produce various particles such as π, K, nuclei and electron. Then the particles create a hadronic and electromagnetic shower and some particles reaches the surface of the earth and others go away.

4.3 Review of Cosmic-ray Observations

Figure 4.1 is the data of the AMS experiment which was performed on the space shuttle Discovery during flight STS-91 in June 1998.[8] Since this data show the dependency of the magnetic latitude, we can determine how the spectral cut-off depends on the geomagnetic field. The BESS experiment[9] were carried out in 1998 by using a balloon for measurements, and the site of observation was near the pole of the geomagnetic field. Therefore the obtained spectra with BESS are less affected by the magnetic field. The form of our model spectrum of comic-ray protons are based on the data of the AMS-98 experiment and BESS-98 experiment[10].

The intensity of cosmic-rays also depends to the altitude of observation point. In general, cosmic-ray intensity becomes small with lower altitude because of the attenuation by the thick atmosphere. Figure 4.2 shows the typical altitude dependence of the cosmic-ray intensity. From this figure, it is there are little difference between the intensity of cosmic-rays in the top of the atmosphere and that in the altitude of the balloon flight.

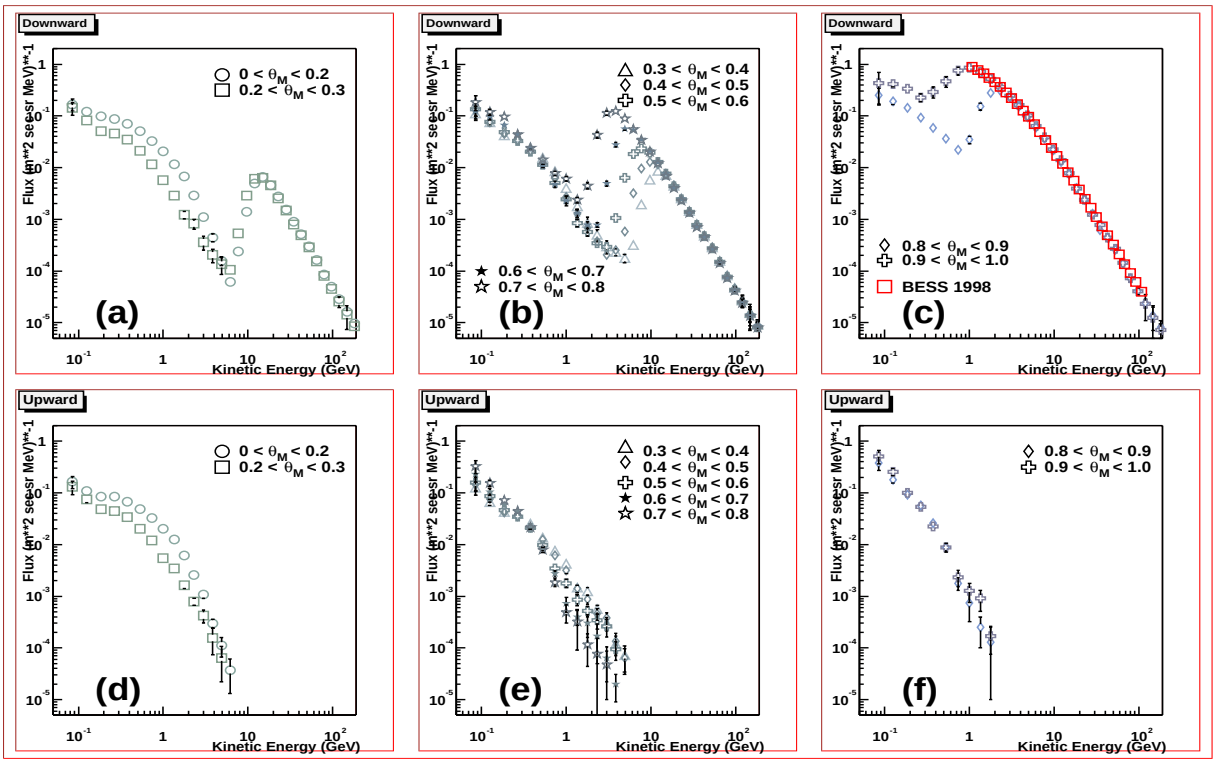

Figure 4.1: Energy spectra of cosmic-ray protons with the AMS experiment. The data of BESS experiment is included in (c).

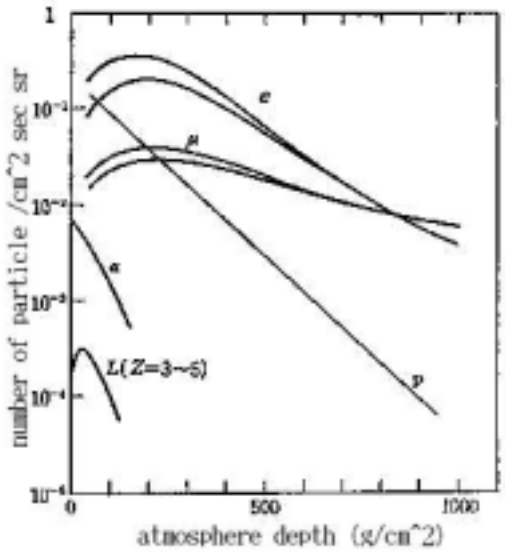

Figure 4.2: An altitude dependency of the cosmic-ray flux

4.4 Modeling of Cosmic-ray Spectra

4.4.1 Cosmic-ray Protons

primary protons We adopted the form of the differential energy spectrum of the intrinsic cosmic-ray protons from outside the solar system as

$$J_{intrinsic}(K) = AR(K)^{-a} \qquad [/\mathrm{m}^2/\mathrm{sec}/\mathrm{sr}/\mathrm{MeV}] \tag{4.4}$$

where $A = 16.9$, $a = 2.79$, and $R(K)$ is a rigidity at its kinetic energy K. We referred to J. Alcaraz et al.[8] for these values. After entering the solar system, particles suffer the influence of the solar wind, so the spectrum is modulated. The geomagnetic field also forms the low energy cut-off in the spectrum. The spectrum modulated by the solar wind is represented by the force-field approximation,

$$J_{modulated}(K, \Phi) = \frac{(K + E_0)^2 - {E_0}^2}{(K + E_0 + \Phi)^2 - {E_0}^2} \times J_{intrinsic}(K + \Phi) \tag{4.5}$$

where Φ is a potential from force-field approximation, K is a kinetic energy, and E_0 is a rest energy of the particle.

Next we included the cut-off by the geomagnetic field as,

$$J_{primary}(K) = J_{modulated}(K, \Phi) \times geomag\_cut(K, K_{cut}) \times \beta(K) \tag{4.6}$$

where K_{cut} is a cut-off energy, $\beta(K)$ is a velocity of the particle in unit of light speed ($\beta = v/c$). The observed flux is represented as a event number per unit volume, and thus $\beta(K)$ is needed. Then the form of $geomag\_cut(K, K_{cut})$ is

$$geomag\_cut(K, K_{cut}) = 1 \Big/ \left(1 + \left(\frac{R(K)}{K_{cut}}\right)^{-12}\right) \tag{4.7}$$

secondary protons The energy spectrum for the secondary protons is modeled, based on the fitting of AMS data:

$$J_{secondary}(K) = 6.0 \times 10^{-3}\, K^{-2.79} e^{-(K/K_b)^{-1}} \qquad [/\mathrm{m}^2/\mathrm{sec}/\mathrm{sr}/\mathrm{MeV}] \tag{4.8}$$

where K is an electron's kinetic energy in unit of [GeV] and $K_b = 0.16$ [GeV].

Figure 4.3 shows how the process described above represents the observed spectrum of $\theta_M = 0.75$.

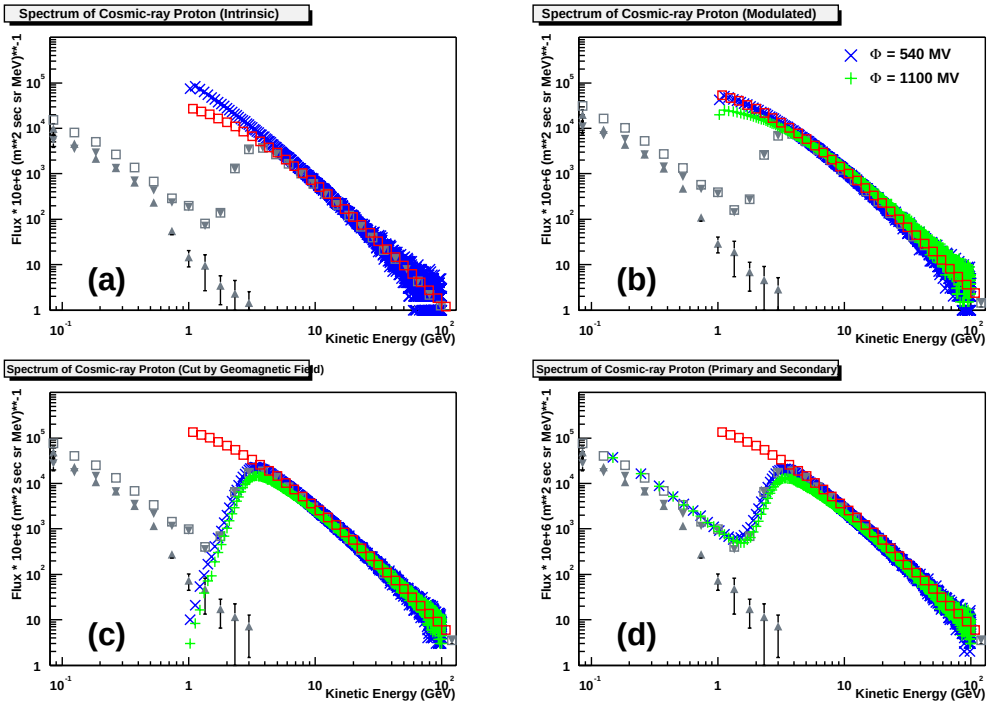

Figure 4.3: Construction of the spectrum of protons: (a) intrinsic spectrum, (b) consider solar modulation, (c) consider geomagnetic cut-off, (d) include secondary spectrum. Cross denotes the spectrucm at solar minimum, plus is at solar maximum, and squares are the data of AMS and BESS.

angular dependency The dependency on the polar angle θ for the cosmic-ray protons is different between the primary and secondary. The intensity of primary protons seem to be almost the same for any incident polar angle in the opposite hemisphere to the earth, and we adopted an uniform distribution against polar angle of primary protons at $0 < \theta < \pi/2$. On the other hand, secondaries depend on the polar angle because of the geomagnetic field. We adopted that the secondary intensity follows $J(\theta) = 1 + 0.6 \sin\theta$ (0 to π) according to the report of Tylka, 2000[12]. As for the azimuthal angle distribution, we assume an uniform distribution (at $0 < \phi < 2\pi$) for both the primary and secondary. We show the angular distribution of simulated protons in figure 4.5.

Finally, we included the flux of protons as $J(K) = J_{primary} + J_{secondary}$ into the simulator. We normalized the intensity of primary and secondary by the ratio of integral value of these differential energy spectrum. Figure 4.4 shows the spectrum we constructed at $\theta_M = 0.65$, $\theta_M = 0.75$, $\theta_M = 0.73$ (at Palestine), together with AMS data. It can be said that our model reproduces the AMS data quite well.

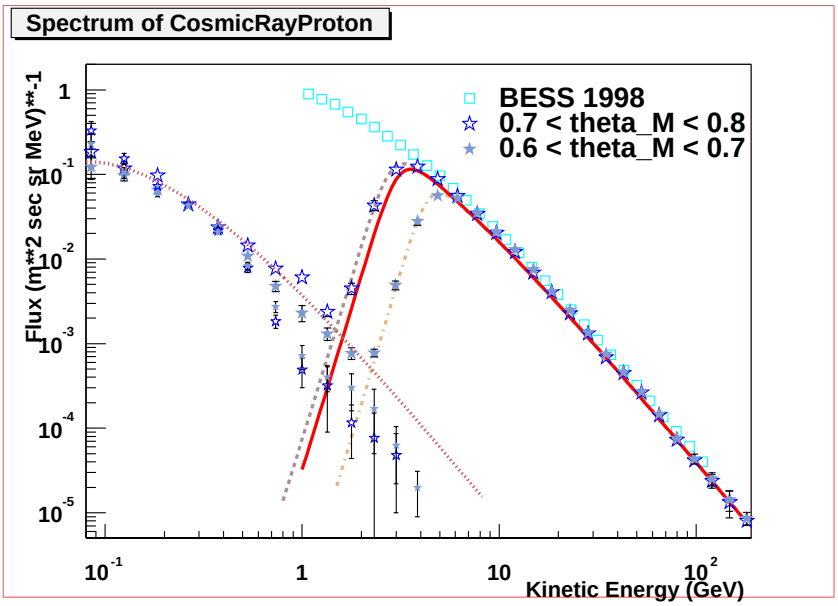

Figure 4.4: Constructed spectrum for $\theta_M = 0.65$ (dashed line), $\theta_M = 0.75$ (dash-doted line), and $\theta_M = 0.73$ (solid line). Real data of BESS experiments are plotted as squares, and that of the AMS data are shown as stars.

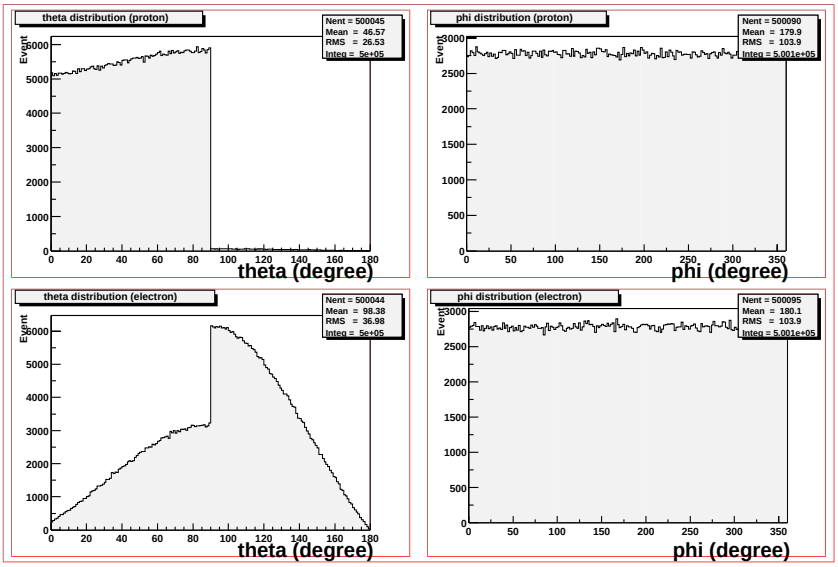

Figure 4.5: Angular distribution of simulated protons (top) and electrons (bottom). The left and right represents a distribution along a polar and azimuthal angle, respectively.

4.4.2 Cosmic-ray Electrons

primary electrons The intrinsic spectrum of the cosmic-ray electrons are represented in the same way as that of protons. The differential energy spectrum of primary electrons is a power law against energies. We adopted the differential energy spectrum of primary electrons from Komori et al.[13]:

$$J_{intrinsic}(K) = AR(K)^{-a} \qquad [/\mathrm{m}^2/\mathrm{sec}/\mathrm{sr}/\mathrm{MeV}], \tag{4.9}$$

where $A = 0.723$, $a = 3.33$ and $R(K)$ is a rigidity of the particle when its energy is K. The solar modulation and geomagnetic cut-off can be considered in the same manner as for protons,

$$J_{modulated}(K, \Phi) = J_{intrinsic}(K + \Phi) \times \frac{(K + E_0)^2 - {E_0}^2}{(K + E_0 + \Phi)^2 - {E_0}^2}, \tag{4.10}$$

$$J_{primary}(K) = J_{modulated}(K, \Phi) \times geomag\_cut(K, K_{cut}) \times \beta(K), \tag{4.11}$$

where $geomag\_cut(K, K_{cut})$ is

$$geomag\_cut(K, K_{cut}) = 1 \Big/ \left(1 + \left(\frac{R(K)}{K_{cut}}\right)^{-12}\right) \tag{4.12}$$

secondary electrons As for the secondary of the cosmic-ray electrons, we referred to the formula based on the balloon experiment by Verma et al., 1967[11] because their experiment was performed at Palestine in Texas, where our balloon experiment will be carried out, and the phase of the 11-year cycle solar activity is nearly the same.

However, their data is restricted to be in the energy range of $10 \leq K \leq 1100$ MeV for splash albedo and $20 \leq K \leq 1250$ MeV for re-entrant albedo, respectively, and the flux calculated from this formula exceeds that of primary electrons in higher energy. Therfore we included a high cut-off energy in the secondary spectrum. We set the index to be the same as that of primary proton spectrum above the cut-off.

After all, the spectrum of secondary electrons becomes:

$$J_{secondary}(K) = AK^{-a} \times \left(1 \Big/ \left(1 + \frac{K}{K_{cut}}\right)^{b-a}\right) \times \beta(K), \tag{4.13}$$

where K [GeV] is a kinetic energy of electron and

$$A = \begin{cases} 2.8 \times 10^{-2} & \text{for re-entrant} \\ 7.3 \times 10^{-2} & \text{for splash} \end{cases}, \quad a = \begin{cases} 1.44 & \text{for re-entrant} \\ 1.29 & \text{for splash} \end{cases}$$
$$b = 2.79, \quad K_{cut} = 0.90 \text{ [GeV]}.$$

Figure 4.6 shows the simulated spectrum of cosmic-ray electrons at Palestine. It can be seen that the secondary electron ratio to the primary is higher than that of protons.

angular dependency We decided the angular dependency of the electrons as the same as protons. That is, the intensity of primary electrons is uniform for the polar angle at $0 < \theta < \pi/2$ and the secondary intensity follows $J(\theta) = 1 + 0.6 \sin\theta$ (0 to π). As shown in figure 4.5 bottom, the secondary is a dominant component unlike protons.

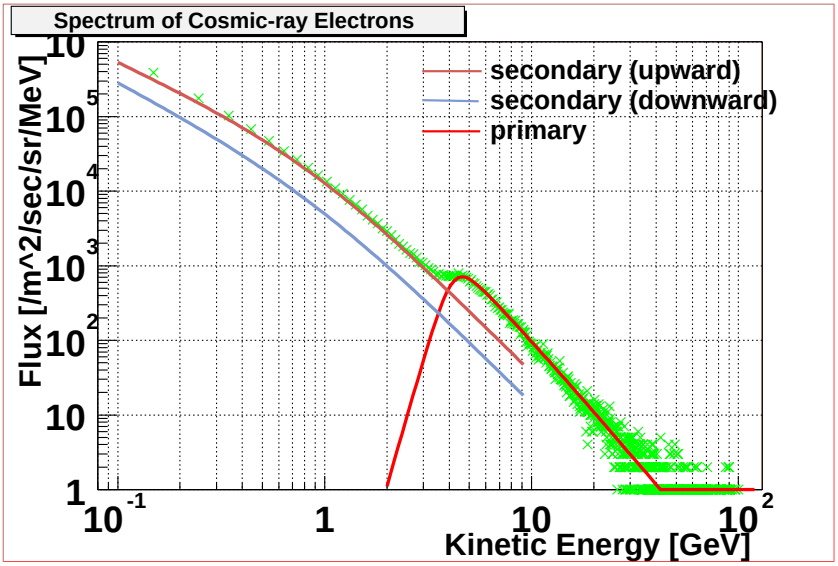

Figure 4.6: The spectrum of cosmic-ray electrons at Palestine. The solid line represents a model included in the simulator, and the crosses are simulated ones.

4.5 Future Plan

We have constructed cosmic-ray flux models at Palestine, but there are still some problems. The spectrum of secondary proton is obtained by fitting the data and does not include the effect of solar modulation or geomagnetic cut-off. The secondary electron flux model can be affected by these effect, and hence we should consider and include those effects by simulating or searching literatures. To construct more accurate simulator of cosmic-rays, the dependency of angle for the cut-off rigidity and the azimuthal angle dependence of the intensity will be considered.

Chapter 5

Prediction of Gamma-ray Flux on the Balloon Experiment

5.1 Balloon Experiment for GLAST

5.1.1 Outline of the Experiment

To test the performance of the detector in a space-like radiation environment, a balloon experiment will be performed in June 2001. In this experiment, the tower which was used for the beam test in 1999 – 2000 is employed, with minor modifications. In addition, plastic scintillators called Active Targets will be placed above TKR. While the well-controlled beam test is a good way to validate the instrument design and calibrate the detector response, a balloon flight will give an opportunity to check the overall design and will reduce mission risks. The objectives of the balloon experiment are summarized as follows;

- Validate the basic detector performance at the single tower level.
- Confirm the data acquisition in the high isotropic background flux of energetic particles.
- Obtain the background event data in an unbiased way that can be utilized as a background data base.

The launch of the balloon will be performed at Palestine in Texas, USA, where some balloon experiments has been carried out in the past. The geomagnetic latitude is $\theta_M = 0.73$ [rad]. After launch, the balloon will reach float altitude at about 120,000 feets in a few hours, and float for about 8 hours at some fixed zenith angles (include horizontal pointing). After finishing the observation, the detector will be detached from the balloon and recovered by using the attached parachute.

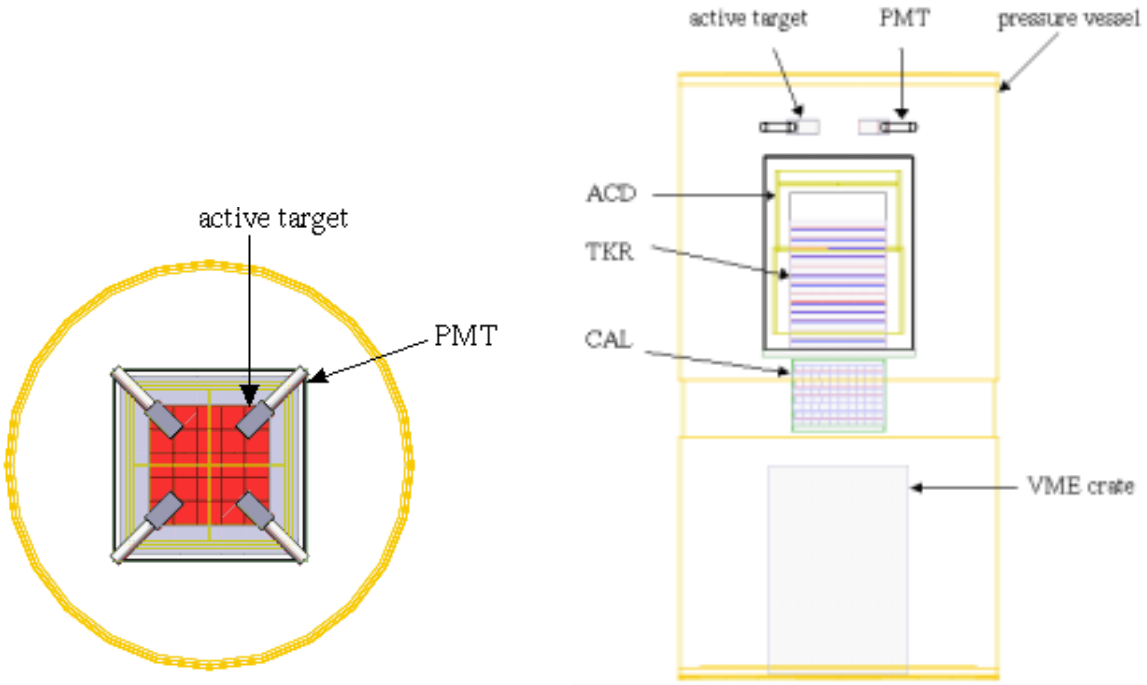

(a) top view

(b) side view

Figure 5.1: Top and side view of the geometry for the balloon experiment constructed in the simulator with Geant4

5.1.2 Instruments specific to the balloon experiment

There are some instruments which is used only in the balloon experiment, such as a Pressure Vessel, Active Targets and a VME crate.

The observation time is limited in the balloon experiment and we want to obtain gamma-rays whose incident direction is known. Thus four Active Targets are put over TKR. When cosmic-ray protons bombard a target, π^0 mesons are created by inelastic scattering, they decay into two gammas immediately. Thus the detector catch the gamma-rays from the targets besides cosmic gamma-rays. Active Targets are made of plastic scintillators whose size is 5 cm $\times$ 5 cm $\times$ 10 cm. The signal from targets is read through photo-multiplier tube (PMT), and will be used as a trigger which is useful to identify the gamma-ray event generated in the Active Target. In the simulator, we placed four rectangular plastic scintillators whose material is Polystyrene (C_8H_8) above TKR as Active Targets. We also placed the magnetic-shield of PMTs of each target as a tube of nickel in the simulator.

In order to minimize the potential problems in the vacuum for the detectors and electronics, the tower and its electronics will be housed in a vessel with a pressure of 1

atmosphere.

Pressure Vessel and VME crate are not directly affect the response of the detector but become a background source, thus we represented these materials as simple shape in the simulator, as shown in Figure 5.1 and Table 5.1.

Material	Elemental composition	Density [g/cm^3]	Size
Active Target	C_8H_8	1.032	5 cm×5 cm×10 cm
PMT (magnetic shield)	Ni	8.85	radius 1.65 cm, length 7.0 cm
Pressure Vessel	Al	2.70	radius 55.44 cm, height 205.8 cm
VME crate	Al	0.54	48.3 cm×48.3 cm×72.2 cm

Table 5.1: Materials added to the balloon simulator

5.1.3 Gamma-rays generated in the balloon

There are two kinds of gamma-rays generated in the balloon, one is generated from π^0's decay which is produced in the Active Target, and the other is generated in any material by various processes, mostly by the bremsstrahlung of electrons. The former is a useful event for the balloon experiment and the latter becomes background. Gamma-rays generated in the material within ACD can easily rejected, therefore the major sources of background are Carbon light-shield walls and Pressure Vessel.

Below we predicted the flux of gamma-rays generated in Active Targets and estimated the number of these "useful event" during the balloon flight.

5.2 Prediction of the Flux of Gamma-ray Generated via π^0-decay in Active Targets

So far we have developed both the cosmic-ray simulator and detector simulator for the balloon experiment. By using them, we can predict the gamma-ray flux on the balloon flight.

5.2.1 Calculation of the number of bombarding protons

At first, we estimated the number of cosmic-ray protons which fall to the detector or four targets during the balloon flight numerically by using the spectral formula of cosmic-rays described in chapter 4. Integrating the differential spectrum of proton, from 1 GeV to 100 GeV for primary and 0.1 GeV to 10 GeV for secondary, we obtained integrated fluxes as follows:

$$A = \int_{1.0}^{100.0} J_{primary}(E)dE = 536.43 \quad [/\mathrm{m}^2/\mathrm{sec}/\mathrm{sr}] \tag{5.1}$$

$$B = \int_{0.1}^{10.0} J_{secondary}(E)dE = 46.916 \quad [/\mathrm{m}^2/\mathrm{sec}/\mathrm{sr}] \tag{5.2}$$

Next, by integrating these values in solid angle we can get the proton flux per unit area and unit time:

$$\begin{aligned} \phi_{primary} &= \int A \; d\Omega \\ &= \int_0^{\pi/2} 2\pi \sin\theta \times A \; d\theta \\ &= 3.37 \times 10^3 \quad [/\mathrm{m}^2/\mathrm{s}], \end{aligned} \tag{5.3}$$

$$\begin{aligned} \phi_{secondary} &= 2 \times \int_0^{\pi/2} 2\pi \times \sin\theta(1 + 0.6\sin\theta) \times B \; d\theta \\ &= 0.78 \times 10^3 \quad [/\mathrm{m}^2/\mathrm{s}], \end{aligned} \tag{5.4}$$

Thus a total flux is $\phi = \phi_{primary} + \phi_{secondary} = 4.15 \times 10^3$ [/m^2/sec].

We generated cosmic-ray protons in such a way that they hit a sphere which radius is a half of the one that circumscribes each target. Total area of the section of the sphere is $4 \times \pi \times (6.1/2)^2 = 117$ cm^2 where the value 6.1 is a radius of the sphere that circumscribes each target. Hence, the count rate of protons which are expected to bombard four Active Targets is 4.15×10^3 [/m^2/sec] $\times 117 \times 10^{-4} = 48.9$ [/sec], or 1.76×10^5 [/hour]. Then total number of those protons during the balloon flight of 8 hours becomes about 1.4×10^6.

5.2.2 Simulation and event selection

We shot 1,000,000 protons into our simulator and selected events that satisfy conditions below. To select gamma-ray events which is caused by π^0 decay, reconstruction of gamma-ray trajectory is needed. But we did not have developed a correct trajectory reconstruction programs yet, thus we prepared these six conditions.

1. 6 continuous hits at SSD in TKR occurred (Level-1 Trigger)
2. more than 50 MeV energy was deposited in one of the target. This criterion is introduced to select events where inelastic scattering occurs.
3. π^0 was created in the target.
4. single conversion of photon occurred in TKR.
5. more than 200 MeV energy was deposited at CAL, in order to select events that can be used for validating the performance of CAL as well as TKR.

6. ratio of the deposited energy at CAL and the energy of gamma-ray is between 0.5 and 1.

Figure 5.2 shows integrated histograms of the number of events satisfying the Level-1 Trigger condition, that where π^0 was generated at target and that where single conversion at TKR occurs. By setting the threshold level of the target at 50 MeV, we can efficiently reject events where an MIP proton passes through the Active Target.

We made a two-dimensional plot of the energy deposited in CAL and (energy deposited in CAL)/(gamma-ray energy) in Figure 5.3, where points within dotted lines meet criteria described above. The number of these "useful events" is 119 for 1M event run, hence over 150 events are expected during the balloon flight.

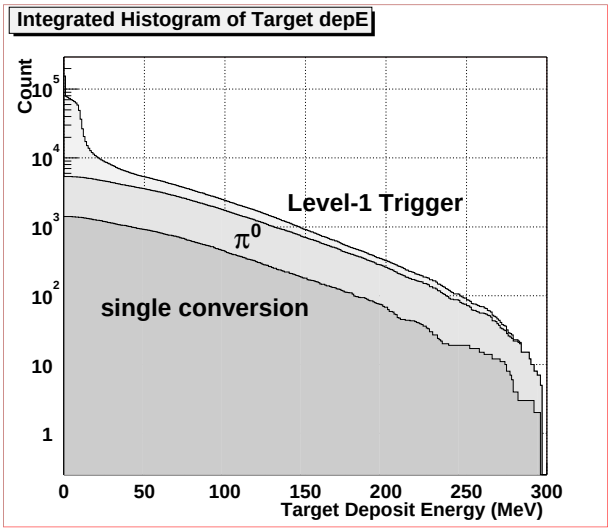

Figure 5.2: An integral histogram of deposited energy of targets

Figure 5.4 shows an example of the event which satisfy the above requirements.

5.3 Future Plan

To complete the simulator for balloon experiment, a few missing components such as a gondola, should be filled because it will be a source of background.

Although we did not estimate this time, it is also needed to estimate the rate of gamma-ray and charged particle background events for the decision of the condition of event selection and trigger. Thus we should perform the simulation shooting the flux of electrons we constructed into the whole detector including Pressure Vessel, and estimate the event rate, energy spectrum, and angular distribution of the background events.

Now we counted gamma-rays from π^0's decay only, but actually there are other events which is regarded as a useful event by the selection we describe above. It seems that these another useful event is also available, thus the estimation of these events is needed.

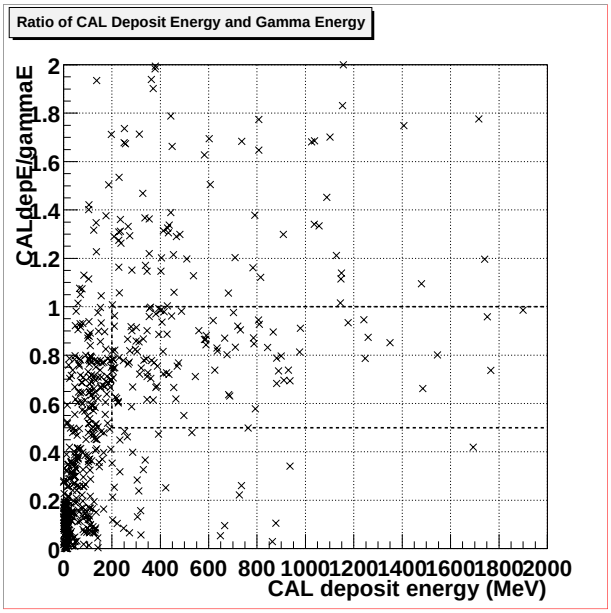

Figure 5.3: Ratio of CAL deposit energy and gamma energy against CAL deposit energy

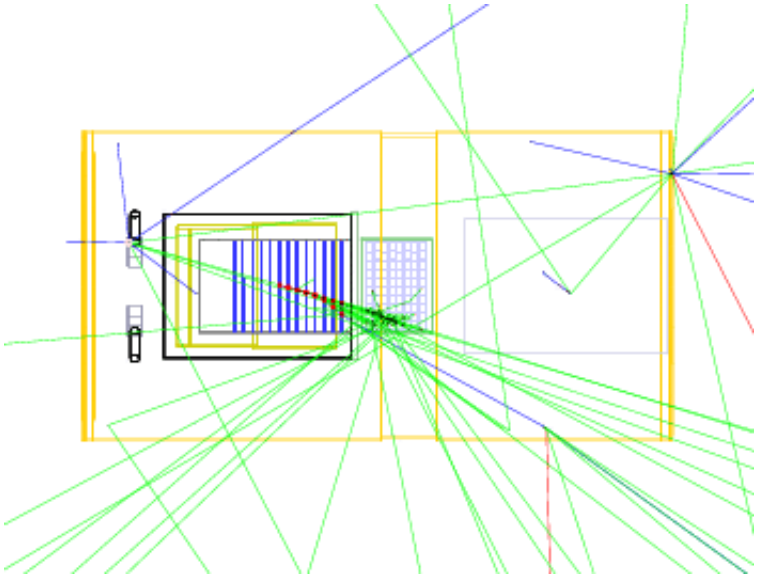

Figure 5.4: An example of "clean" gamma event

Chapter 6

Summary

We developed a detector simulator and a cosmic-ray generator for GLAST, especially for the balloon experiment, in the framework of Geant4. The detector simulator well represent the tower geometry of a beam test and that of balloon experiment in the detail sizes and materials, and its validity is checked. We also constructed the cosmic-ray event generator of protons and electrons based on the past experiments. The cosmic-ray generator is considered effects of solar modulation and geomagnetic cut-off, thus it represents the cosmic-ray flux in the balloon experiment well. Using these simulators, we estimated the count rate of useful gamma-ray events which is generated via π^0 decay from the inelastic scattering in Active Targets. As a result, we found that more than 300 useful events will be observed during the 8-hour balloon flight.

We considered gamma-rays from π^0's decay only, so it seems that more useful events are found in balloon experiment considering gamma-rays generated by other processes. This time we did not perform the estimation of gamma-ray background and charged particle background yet. Continuous study and simulation is needed for a success of the balloon experiment and GLAST flight model.

Acknowledgement

I would like to express my thanks to Prof. T. Ohsugi and Prof. T. Kamae for their continuous support. Special thanks are due to Prof. Y. Fukazawa, Dr. T. Mizuno, and Dr. M. Ozaki for their guidance on my study. Without their instruction, this thesis would not finished. Thanks are due to Dr. Y. Iwata and Dr. S. Yoshida for their advice about my study.

I wish to thank to Dr. T. Handa, Mr. T. Ohmoto, Mr. H. Ohyama, Mr. H. Yamamoto, Mr. N. Nakao and Mr. T. Masuda for their advice and useful discussion. I also thank to Mr. S. Ogata, Mr. H. Mizushima, and all the members of High Energy Physics Laboratory in Hiroshima University, and GLAST group of Stanford Linear Accelerator Center.

Bibliography

[1] GLAST Home Page at Stanford University, http://glast.stanford.edu/

[2] Geant4 Home Page, http://wwwinfo.cern.ch/asd/geant4/geant4.html

[3] E. do Couto e Silva et al., Result from the Beam Test of the Engineereing Model of the GLAST Large Area Telescope, Oct. 2000.

[4] GLAST Testbeam Users guide, Jan. 2000.

[5] Geometry for the TRACKER to update .XML, http://www-glast.slac.stanford.edu/testbeam/geometrytkr.ppt

[6] The European Physical Journal C, 2000.

[7] D. Thompson, GLAST Balloon Flight Engineering Model - Plan for Balloon Flight (DRAFT), 2000.

[8] J. Alcaraz et al., Protons in near earth orbit, Phys. Let. B 472(2000) 215-226.

[9] T. Sanuki et al., Precise Measurement of Cosmic-Ray Proton and Helium Spectra with the BESS Spectrometer, astro-ph/0002481, 2000.

[10] M. Ozaki, Cosmic Ray spectrum estimation for the GLAST balloon flight in June 2001, GLAST internal report.

[11] S. D. Verma, Measurement of the Charged Splash and Re-Entrant Albedo of the Cosmic Radiation, Journal of Geophysical Research, 1967, Vol 72.

[12] A. J. Tylka, A Review of Cosmic-Ray Albedo Studies: 1949-1970, GLAST internal report.

[13] Y. Komori et al., ECC による 99 年度高エネルギー一次電子の観測, 大気球シンポジウム, Pg 33-36.

[14] L. J. Gleeson et al., Solar Modulation of Galactic Cosmic Rays, 1968, ApJ, 154, 1011.

[15] T. Mizuno et al, Geant4 Simulation for GLAST Beam Test (99) and Balloon Test Flight, 2001.

[16] S. Ogata et al., 2001.

[17] Y. Sato, 2001, graduate thesis.

[18] Y. Azechi, 2001, graduate thesis.